

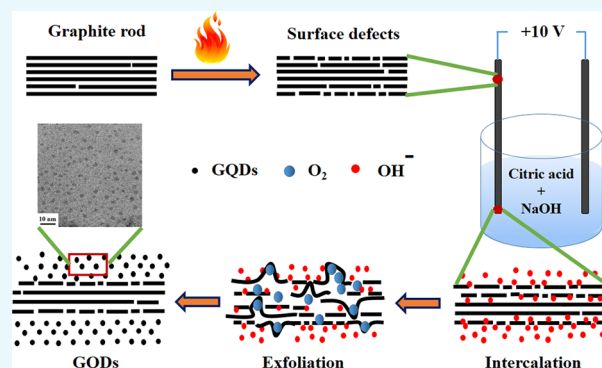
# Electrochemical Method To Prepare Graphene Quantum Dots and Graphene Oxide Quantum Dots

Satyaprakash Ahirwar,<sup>1</sup> Sudhanshu Mallick,<sup>1</sup> and Dharendra Bahadur<sup>1\*</sup>

Department of Metallurgical Engineering and Materials Science, Indian Institute of Technology Bombay, Mumbai 400076, India

## Supporting Information

**ABSTRACT:** In this study, we present the preparation of graphene quantum dots (GQDs) and graphene oxide quantum dots (GOQDs). GQDs/GOQDs are prepared by an easy electrochemical exfoliation method, in which two graphite rods are used as electrodes. The electrolyte used is a combination of citric acid and alkali hydroxide in water. Four types of quantum dots, GQD1–GQD4, are prepared by varying alkali hydroxide concentration in the electrolyte, while keeping the citric acid concentration fixed. Variation of alkali hydroxide concentration in the electrolyte results in the production of GOQDs. Balanced reaction of citric acid and alkali hydroxide results in the production of GQDs (GQD3). However, three variations in alkali hydroxide concentration result in GOQDs (GQD1, GQD2, and GQD4). GOQDs show tunable oxygen functional groups, which are confirmed by X-ray photoelectron spectroscopy. GQDs/GOQDs show absorption in the UV region and show excitation-dependent photoluminescence behavior. The obtained average size is 2–3 nm, as revealed by transmission electron microscopy. X-ray diffraction peak at around  $10^\circ$  and broad D band peak at  $1350\text{ cm}^{-1}$  in Raman spectra confirm the presence of oxygen-rich functional groups on the surface of GOQDs. These GQDs and GOQDs show blue to green luminescence under 365 nm UV irradiation.



## 1. INTRODUCTION

Graphene is a single carbon atom thick layer, in which  $sp^2$  carbon atoms are densely packed in a two-dimensional honeycomb lattice. It has exceptional electronic, thermal, and mechanical properties. These properties of graphene are extensively used in various applications, such as solar cells, supercapacitors, biosensors, and so forth.<sup>1,2</sup>

Graphene quantum dots (GQDs) or graphene oxide quantum dots (GOQDs) are zero-dimensional graphene/graphene oxide nanomaterials with remarkable luminescence properties associated with edge effects or defect states (i.e., surface states).<sup>3–6</sup> Surface states enable excitation-dependent photoluminescence (PL) behavior. Surface states, such as oxygen-rich functional groups, allow GQDs to be dispersed in the solvents. As a result, GQDs/GOQDs have a great potential toward optical and electrochemical sensing,<sup>7,8</sup> photovoltaics,<sup>7</sup> photocatalysis,<sup>8</sup> bioimaging,<sup>9,10</sup> biosensing,<sup>10,11</sup> light-emitting diodes,<sup>12</sup> and so forth. These can be synthesized by top-down or bottom-up methods. Usually, top-down methods cut carbon fibers, graphene sheets, graphene electrode, graphite powder, plant materials, such as mango leaves, into GQDs/GOQDs, respectively, by chemical oxidation and exfoliation,<sup>13</sup> hydrothermal synthesis,<sup>14</sup> electrochemical synthesis,<sup>15</sup> UV-assisted synthesis,<sup>16</sup> and microwave synthesis.<sup>17</sup> Bottom-up methods include molecular precursors (natural or artificial) to construct GQDs/GOQDs by carbonization of citric acid,<sup>18,19</sup> cage-

opening of fullerene,<sup>20</sup> microwave carbonization and aromatization by acetylacetone,<sup>21</sup> microwave-assisted hydrothermal process,<sup>22</sup> microwave-assisted pyrolysis of polyethylene glycol and saccharide,<sup>23</sup> polycyclic aromatic hydrocarbons,<sup>24,25</sup> microwave-assisted heating of carbon nanotubes,<sup>26</sup> chemical exfoliation of graphite nanoparticles,<sup>27</sup> and so forth.

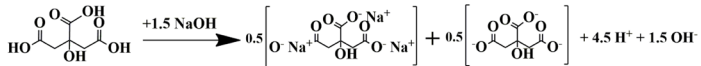
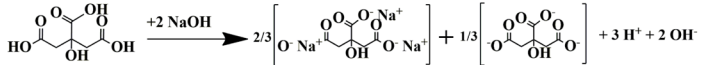
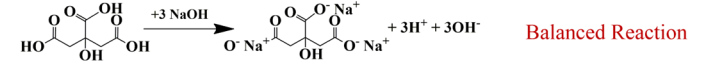
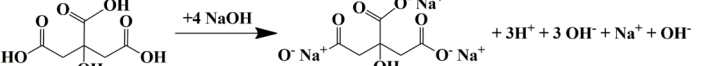
Most of the top-down techniques involve strong chemicals and tedious synthesis protocols, whereas the bottom-up techniques, generally, require special equipment and are time-consuming processes. Hence, there is a need of a simple, efficient, and affordable method for the synthesis of GQDs and GOQDs. In this work, we report a new facile synthesis route to prepare GQDs and GOQDs from graphite rod via electrochemical exfoliation, in which the electrolyte is a combination of a weak acid and a strong alkali hydroxide. This methodology ensures an easy approach toward the synthesis of GQDs and GOQDs, which is quite similar to electrochemical preparation of tungsten disulfide quantum dots and molybdenum disulfide quantum dots.<sup>28,29</sup> The steps for preparing the GQDs and GOQDs are essentially the same. The GOQDs are obtained by varying the concentration of NaOH in the electrolyte. The variation of the concentration of NaOH causes the predefined

Received: October 12, 2017

Accepted: November 13, 2017

Published: November 28, 2017

Table 1. Electrolyte, Chemical Reactions, and Anion Distributions for Obtaining the GQD1–GQD4

	Electrolyte	Chemical Reaction	Anion Distribution
GQD1	1M Citric + 1.5M NaOH		1.5 OH <sup>-</sup> + 0.5 Citrate ions
GQD2	1M Citric + 2M NaOH		2 OH <sup>-</sup> + 0.3 Citrate ions
GQD3	1M Citric + 3M NaOH		3 OH <sup>-</sup>
GQD4	1M Citric + 4M NaOH		4 OH <sup>-</sup>

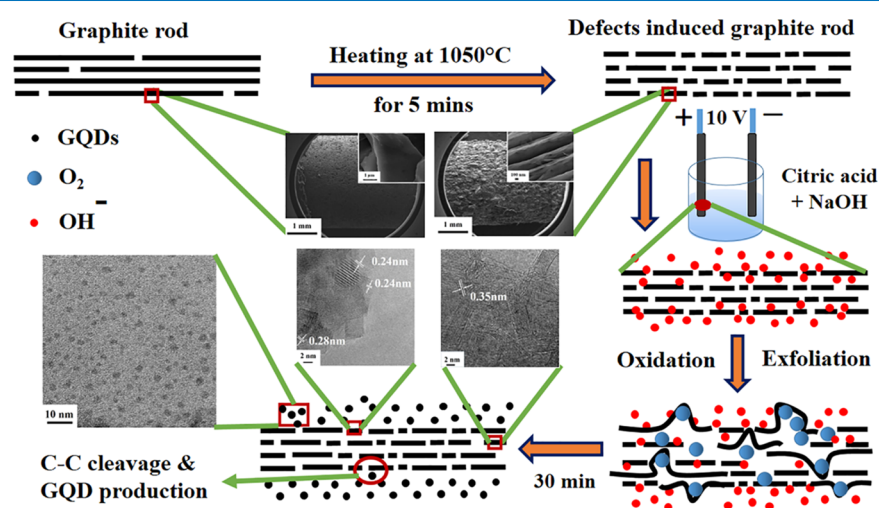


**Figure 1.** Schematic illustration of electrochemical exfoliation of defect-induced graphite rod. Intercalation of OH<sup>-</sup> ions, O<sub>2</sub> production, and exfoliation process result in the production of graphene quantum dots.

molar ratio to vary. As a result, oxygen-rich functional groups are produced in the GQDs, which are known as GOQDs. So, this electrochemical exfoliation method is easy and able to produce very small GQDs and GOQDs with the size of ca. 2–3 nm. The novelty of the present work is generating defects on the surface of graphite rod by heating it at high temperature. These defects facilitate the electrochemical exfoliation process by providing more number of sites for oxidation and exfoliation. Second, variation of NaOH concentration in the electrolyte results in the production of GQDs/GOQDs with different structural and optical properties.

## 2. CLASSIFICATION, MECHANISM OF GQDS/GOQDS FORMATION, AND ROLE OF ANION

**2.1. Classification of Prepared GQDs Based on Electrolyte.** Here, in the electrochemical setup, two graphite rods were dipped in the electrolyte. By varying the electrolyte concentration, quantum dots with varying oxygen functionalization were formed. Classification of prepared GQDs/GOQDs on the basis of electrolyte concentration is shown in Table 1. For the convenience of the readers, these four samples are referred in the text as GQD1–GQD4.

GQD1, GQD2, GQD3, and GQD4 are obtained with the predefined molar ratios of citric acid to NaOH of 1:1.5, 1:2, 1:3, and 1:4, respectively. The obtained anion distribution is given

in Table 1. For GQD1 and GQD2, we decrease the concentration of NaOH to 1/2 and 2/3 times as compared to balanced reaction (GQD3). For GQD4, we increase the concentration of NaOH to 4/3 times as compared to balanced reaction (GQD3). By varying the concentration of NaOH in the molar ratio, GOQDs (GQD1, GQD2, and GQD4) can be obtained. The range of NaOH in the predefined molar ratio can be 1.5–4, if the citric acid is constant at 1. Thus, GQD3 is GQDs, and GQD1, GQD2, and GQD4 are GOQDs.

### 2.2. Mechanism: From Graphite Rod to GQDs.

Schematic illustration of the preparation of GQDs by electrochemical exfoliation process is shown in Figure 1. The bare graphite rods are taken as starting material. The scanning electron microscopy (SEM) image of the surface of the bare graphite rod shows typical graphite structure, in which the sheets are large and densely packed. Then, these bare graphite rods are heated at 1050 °C for 5 min. The SEM image of graphite rod post heating results in the creation of numerous defects on the surface of the graphite rods (we call it as defect-induced graphite rod). During electrochemical exfoliation process, cutting and oxidation occur at defect sites. So, generating more number of defects will provide more sites for cutting and oxidation and facilitate the process. The defect-induced graphite rods are used as anode and cathode and then dipped in the electrolyte solution. Electrolyte used is a mixture

of citric acid and NaOH in water. This results in sodium citrate salt and water in the solution. On applying potential, hydrolysis of water occurs, giving  $H^+$  and  $OH^-$  ions. Due to the influence of the electric field, there is intercalation of anions ( $OH^-$  ions) in between the graphite layers of the defect-induced graphite rod. The  $OH^-$  ions get oxidized on the defect sites. The produced oxygen creates pressure in between the graphite layers. The  $OH^-$  ions and oxygen occupy the van der Waals gaps and results in exfoliation of the defect-induced graphite rod (anode). Due to C–C cleavage by the electric field, either GQDs or GOQDs are obtained based on the predefined molar ratio of citric acid and NaOH.<sup>30–37</sup> Schematic illustration (Figure 1) depicts the surface of graphite rod before and after heating, the formation of  $OH^-$  ions, intercalation of  $OH^-$  ions, production of oxygen, and the obtained GQDs. The transmission electron microscopy (TEM) image of inside core of graphite rod (Figure 1) shows a typical graphite structure, in which the separation between layers is 0.35 nm. Other TEM image shows the surface of graphite rod after electrochemical exfoliation process, in which the sites are shown from where the GQDs were cut and peeled off. These sites show that the separation between layers is 0.23 nm, which is the lattice constant of GQDs or graphene. The final TEM image (Figure 1) shows the distribution of obtained GQDs prepared by electrochemical exfoliation process.

**2.3. Role of Anion Concentration in the Electrolyte for GQDs and GOQDs Formation.** The anion distribution is given in Table 1. GQD1: The obtained 1.5 M  $OH^-$  ions and 0.5 M citrate ions move toward the anode and oxidize. As the hydroxyl ion concentration is half (1.5 M  $OH^-$  ions), in comparison to that of GQD3 (3 M  $OH^-$  ions; balanced reaction), this should result in decrease in oxidation. However, from the characterization results, it is apparent that a large amount of oxidation occurs. This is due to the participation of citrate ions in the oxidation and peeling off process. Here, GOQDs are obtained instead of GQDs. GQD2: The obtained 2 M  $OH^-$  ions and 0.3 M citrate ions move toward the anode and oxidize. As the hydroxyl ion concentration is 2/3 (2 M  $OH^-$  ions) in comparison to that of GQD3 (3 M  $OH^-$  ions), this should result in decrease in oxidation. However, characterization results suggest that the occurrence of oxidation is less than that for GQD1 but more in comparison to that of GQD3 (balanced reaction). This is because of the decrease in citrate ions. Here, GOQDs are obtained with a lesser amount of oxygen functional groups in comparison to that of GQD1. GQD3: The obtained 3 M  $OH^-$  ions move toward the anode and oxidize. As a result, the 3 M  $OH^-$  ions start peeling off the graphite layers from the defect sites. Here, GQDs are obtained. GQD4: As the  $OH^-$  ion concentration is higher (4 M  $OH^-$  ions), in comparison to that of GQD3 (3 M  $OH^-$  ions), there is an increase in oxidation, which is confirmed by the characterization results. This is because of the increase in hydroxyl ions. Here, GOQDs are obtained instead of GQDs.

### 3. RESULTS AND DISCUSSION

Figure 2 shows GQD1–GQD4 images before (a–d) and after (e–h) electrochemical exfoliation and daylight/under 365 nm UV irradiation (i–l).

**3.1. TEM.** Figure 3 shows TEM images depicting size distribution of GQD1–GQD4; the inset images depict high-resolution images of GQD1–GQD4 and the corresponding size distribution curves. Table S1 depicts the values obtained by TEM characterization. The average sizes of GQD1–GQD4 are

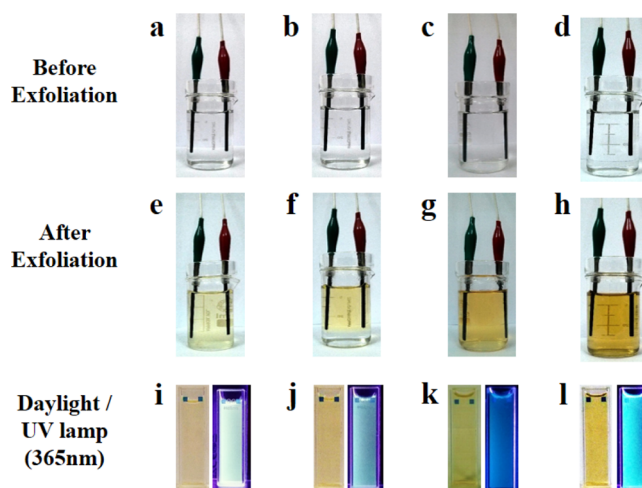


**Figure 2.** Images of GQD1–GQD4 before (a–d) and after (e–h) electrochemical exfoliation and daylight/under 365 nm UV irradiation images for GQD1–GQD4 (i–l).

in the range of 2.24–3.04 nm, with the size distribution in the range of 1.5–4.5 nm. The inset images depict the high-resolution TEM images of GQDs, in which the interplanar spacing of ca. 0.21 nm is observed. GQD1–GQD4 with a lattice spacing of  $\sim 0.21$  nm correspond to the (100) hexagonal lattice spacing along the [001] direction present in the graphene structure.<sup>38</sup>

**3.2. X-ray Photoelectron Spectroscopy (XPS).** Figure 4 illustrates XPS survey peaks and high-resolution  $C_{1s}$  spectra for GQD1–GQD4. Table 2 depicts the XPS survey peaks and C%, O%, and  $C_{1s}$  deconvoluted peaks. XPS is used to analyze the composition of prepared GQDs. The XPS survey scans of GQD1–GQD4 depict two peaks, for  $C_{1s}$  at ca. 284.4 eV and  $O_{1s}$  at ca. 531.2 eV. For GQD1–GQD4, atomic percentage of  $C_{1s}$  is in the range of 39.6–54.4% and atomic percentage of  $O_{1s}$  is in the range of 45.6–60.4%. The narrow scan of  $C_{1s}$  band for GQD1 and GQD3 can be fitted to four deconvoluted characteristic peaks, whereas GQD2 and GQD4 can be fitted to five deconvoluted characteristic peaks. The deconvoluted characteristic peaks correspond to the binding energies of C–C, C=C, C–H, C–O, C=O, and O–C=O bonds. The binding energy observed for C–C is 283.85 eV, C=C is 284.4 eV, C–H is  $285.2 \pm 0.1$  eV, C–O is  $286.8 \pm 0.2$  eV, C=O is  $287.8 \pm 0.1$  eV, and O–C=O is 288.57 eV.<sup>39</sup>

From GQD1 to GQD3, O% decreased from 60.4 to 45.6%. This implies that the oxidation has decreased. This is due to decrease in citrate ions from GQD1 (0.5 M) to GQD3 (0 M). However, from GQD3 to GQD4, O% increased from 45.6 to 57.1%. This is due to the increase in  $OH^-$  ions from GQD3 (0.3 M) to GQD4 (0.4 M). This results in increase in oxidation. The amount of C–O functional group in GQD1 is maximum (36.9%) and in GQD3 is minimum (12.6%). The amount of C–O functional group in GQD2 (19.4%) is comparable to that in GQD4 (18.4%). The amount of C=O functional group in GQD1 is maximum (14.5%) and that in GQD4 is minimum (5.1%). The O–C=O (2.5%) functional group is observed only in GQD4.<sup>40</sup> GQD1 and GQD4 were observed to be having maximum amount of oxygen functional groups.<sup>41–43</sup> The amount of oxygen functional groups is more in GQD1, GQD2, and GQD4 in comparison to GQD3. This shows that during electrochemical exfoliation reaction, oxygen-rich functional groups are introduced onto the surface of



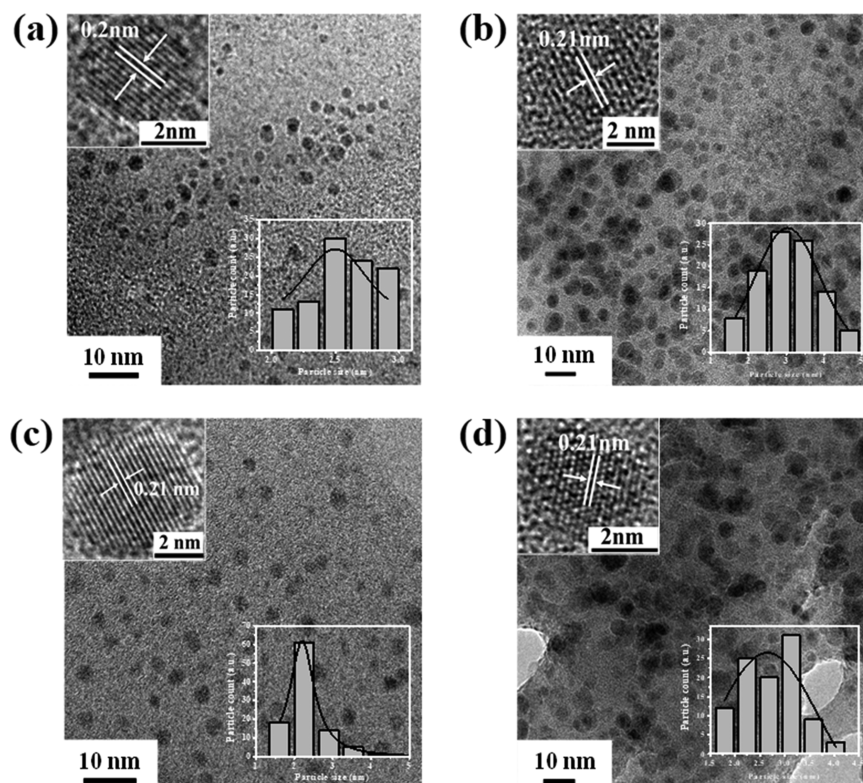


**Figure 3.** TEM images showing size distribution of GQD1–GQD4 (a–d) (scale bar, 10 nm). The inset images show high-resolution images of GQD1–GQD4 (scale bar, 2 nm) and the corresponding size distribution curves.

GQDs. The presence of the oxygen-rich functional groups in GQDs results in green luminescence under 365 nm UV irradiation (Figure 2) and broadening of D band in Raman spectra (Figure 6).

**3.3. X-ray Diffraction.** Figure 5 illustrates X-ray diffraction patterns of GQD1–GQD4. As depicted in Figure 5, GQD1–GQD4 exhibit a broad diffraction peak at ca.  $23^\circ$  corresponding to the (002) plane.<sup>44</sup> It is to be noted that GQD1, GQD2, and GQD4 also show another diffraction peak at ca.  $9^\circ$ . This implies the presence of oxygen-rich functional groups present on the surface of GQD1, GQD2, and GQD4. However, this peak is negligible for GQD3, which indicates that the presence of oxygen functional groups is minimal.<sup>45</sup>

**3.4. Raman Spectroscopy.** Figure 6 illustrates Raman spectra of GQD1–GQD4. Table S2 depicts the values obtained by Raman characterization. Two characteristic peaks were observed, which correspond to D and G bands. For GQD1–GQD4, the D band is observed at ca.  $1350\text{ cm}^{-1}$  and G band at ca.  $1590\text{ cm}^{-1}$  with  $I_D/I_G$  greater than 1.

The values of D band, G band, and  $I_D/I_G$  are shown in Table S2. D band is a disorder-induced band, which confirms the presence of disorder on the edges in the form of  $sp^3$  carbons, surface states, or functional groups on the surface of GQDs. The D band observed here is in the range of  $1338\text{--}1350\text{ cm}^{-1}$ . It arises due to bonding and antibonding orbitals, i.e., intervalley backscattering with breathing mode of  $A_{1g}$  phonon at  $K$ -point. The broadening of the D peak is due to an increase in  $sp^3$  hybridized content of carbon to carbon bonds, carbon to oxygen bonds, epoxy and hydroxyl groups, and so forth.<sup>46</sup> The G band arises due to the stretching C–C bonds present in the  $sp^2$  carbon network. The G band observed here is in the range of  $1585\text{--}1598\text{ cm}^{-1}$ . This is due to  $E_{2g}$  phonon vibrations at  $\Gamma$ -point, which arises due to strains produced in the  $sp^2$  carbon

network. Intensity ratio of D band to G band, i.e.,  $I_D/I_G$ , is the measure of degree of disorder.<sup>47</sup> The  $I_D/I_G$  observed is greater than 1. This indicates that several defects are present at the surface of GQDs.

**3.5. UV–Vis and Photoluminescence Excitation (PLE) Spectra.** Figure 7 illustrates UV–vis spectra and PLE spectra for GQD1–GQD4 (a–d). The inset images depict GQD1–GQD4 in daylight and under 365 nm UV irradiation. Table 3 depicts the values for different transitions and the band gap obtained. GQD1–GQD4 dispersions emit light yellow fluorescence in daylight. When exposed to 365 nm UV irradiation, GQD1–GQD4 emit light green, light blue-green, blue, and blue-green regions, respectively.

A prominent absorption peak is observed between 253 and 279 nm, which corresponds to  $\pi \rightarrow \pi^*$  transition of  $sp^2$  C–C bonds. The shoulder peak at around 325–370 nm ascribes to  $n \rightarrow \pi^*$  transition of C=O bonds or other functional groups present on the surface of GQD1–GQD4.<sup>6</sup> Two prominent peaks are observed in the PLE spectra between 343 and 403 nm, which correspond to armchair edges and oxygen-rich functional groups present on the surface of GQD1–GQD4.<sup>48</sup> These surface defects or oxygen-rich functional groups on GQD1–GQD4 emit blue to green fluorescence when exposed to 365 nm UV irradiation.

**3.6. Excitation-Dependent Photoluminescence Behavior.** Figure 8 illustrates excitation-dependent PL behavior of GQD1–GQD4, respectively. Table S3 depicts the values obtained by PL characterization. From UV–vis spectra and PLE spectra, it is identified that the excitation wavelength is in the range of 343–403 nm. The excitation wavelength has been varied between 350 and 510 nm with an increment of 20 nm. A variation of the excitation wavelength causes a change in



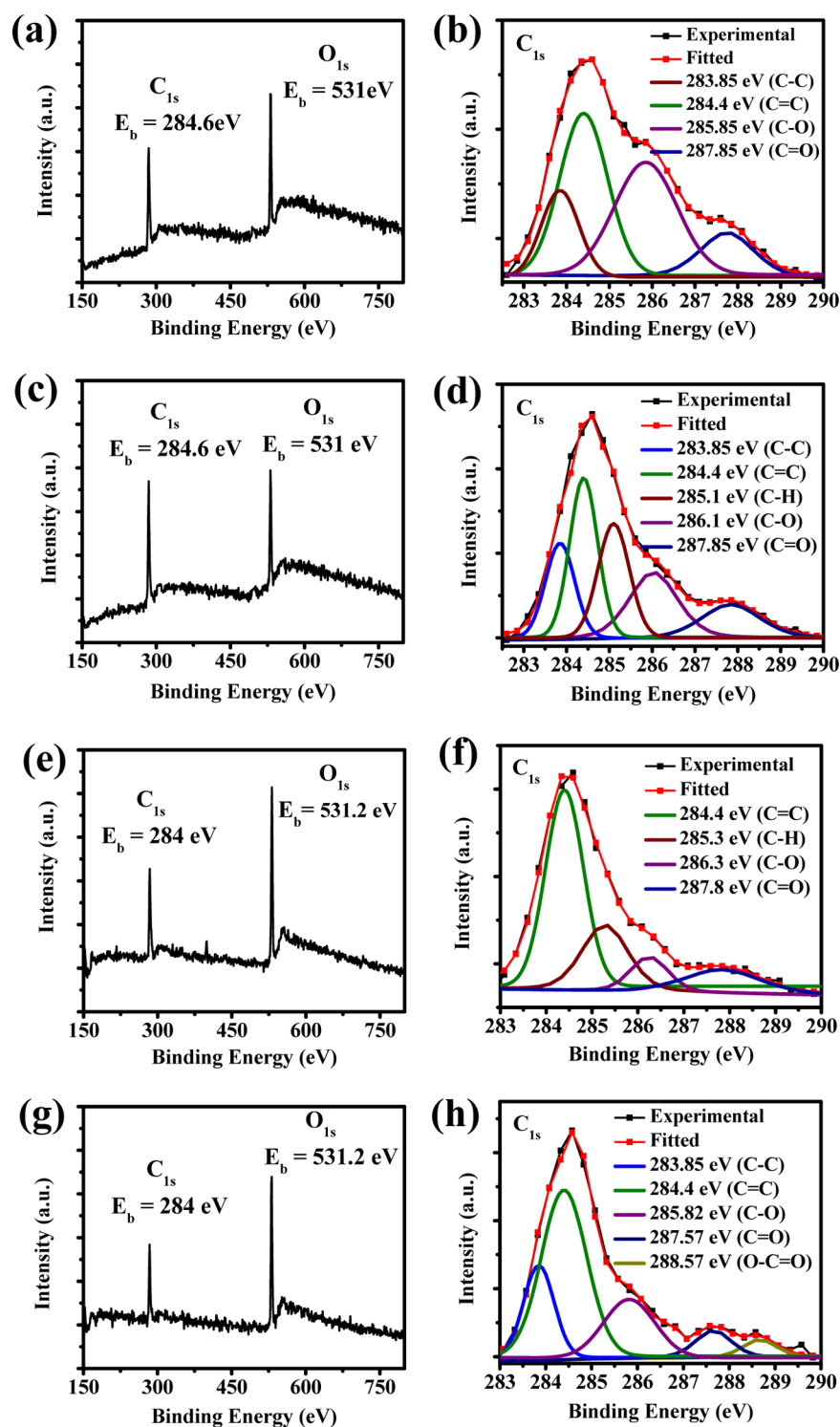


Figure 4. XPS survey peaks for GQD1–GQD4 (a, c, e, g). High-resolution C<sub>1s</sub> spectra peaks for GQD1–GQD4 (b, d, f, h).

Table 2. XPS Survey Peak Values, High-Resolution C<sub>1s</sub> Spectra Peaks Values, and the Corresponding Binding Energies and Atomic Percentage

	C <sub>1s</sub> (At. %)	O <sub>1s</sub> (At. %)	C–C (At. %)	C=C (At. %)	C–H (At. %)	C–O (At. %)	C=O (At. %)	O–C=O (At. %)
	284.4 eV	531.2 eV	283.85 eV	284.4 eV	285.2 ± 0.1 eV	286.8 ± 0.2 eV	287.8 ± 0.1 eV	288.57 eV
GQD1	39.6	60.4	17.2	39		36.9	14.5	
GQD2	44.1	55.9	16.7	27.4	21.9	19.4	11.7	
GQD3	54.4	45.6		62.5	23.2	12.6	15.2	
GQD4	42.9	57.1	17.7	48.3		18.4	5.1	2.5

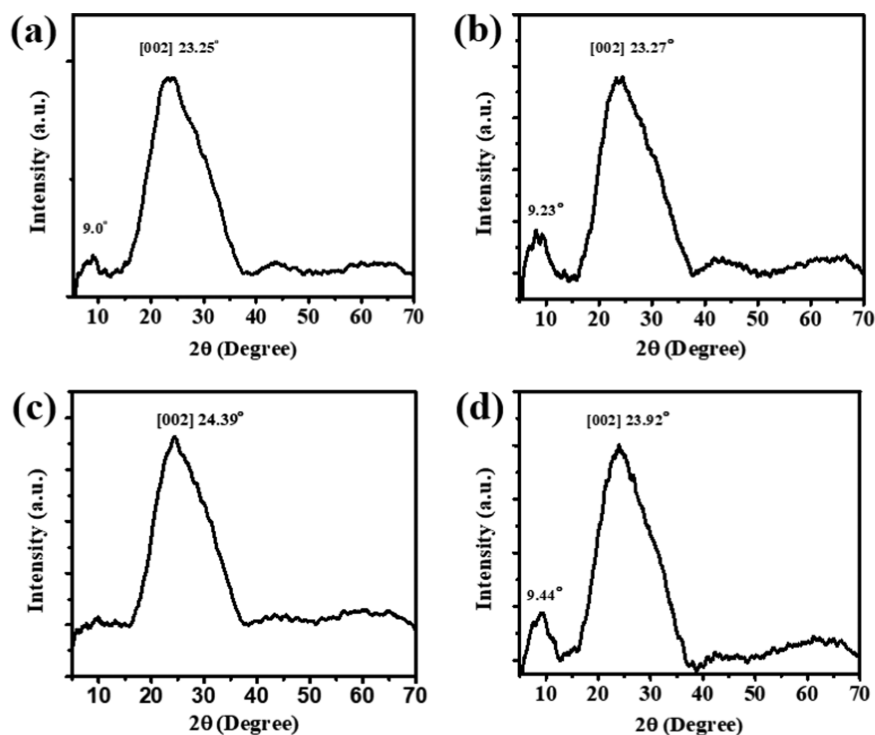


Figure 5. X-ray diffraction patterns of GQD1–GQD4 (a–d).

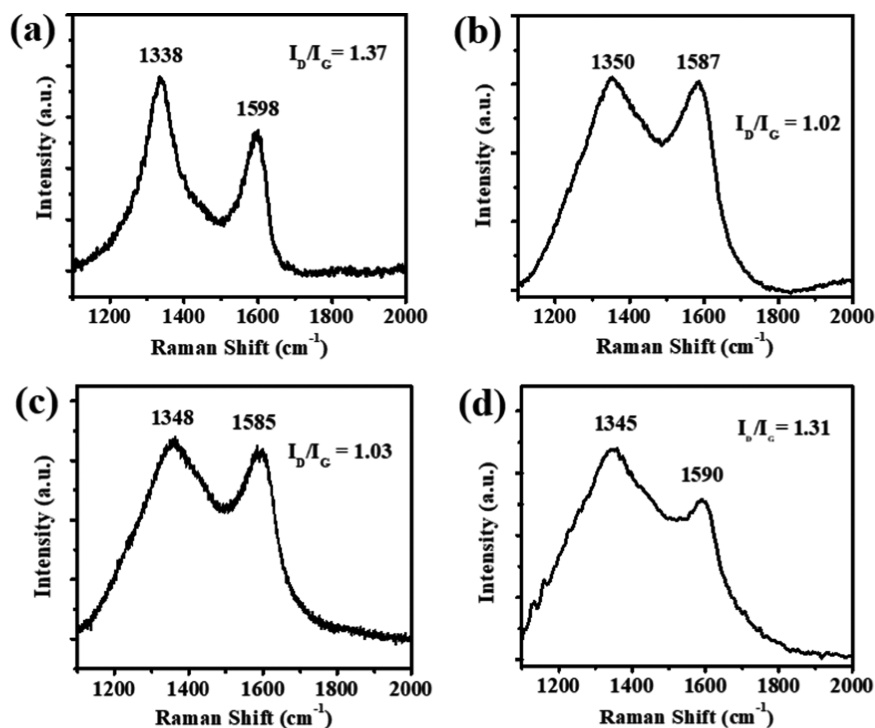
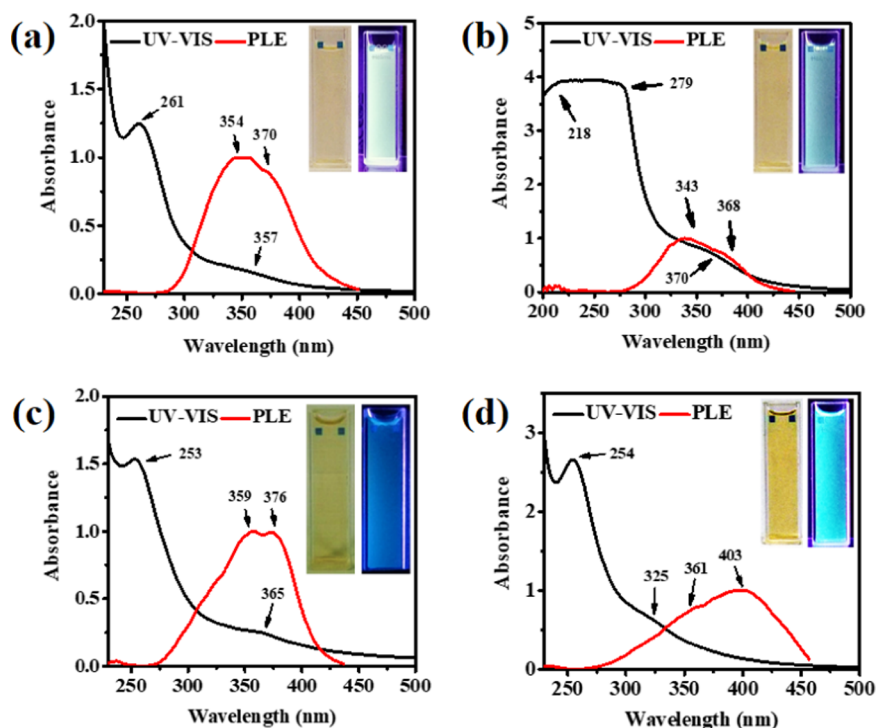


Figure 6. Raman spectra of GQD1–GQD4 (a–d) measured with 514 nm argon laser at 10 mW power. D band and G band are observed at ca. 1350 and 1590  $\text{cm}^{-1}$ , respectively.

emission wavelength. The peak intensity of emission reduces with an increase of the excitation wavelength.

PL in GQDs arises due to quantum confinement effect and surface states.<sup>6</sup> Quantum confinement effect is due to carbon core. Surface states are due to the presence of functional groups present on the surface of GQD1–GQD4. XPS images (discussed in Figure 4) suggest the presence of C–H, C–O,

C=O, and O–C=O functional groups on the surface of GQD1–GQD4. These groups significantly contribute to the luminescence of GQD1–GQD4. Variation in excitation wavelength causes a change in emission wavelength. This could be due to differently sized GQDs (Figure 3) and surface states (Figure 4).<sup>6</sup> PL spectrum for GQD1 exhibits two peaks at 460 and 522 nm. The peak at 460 nm could possibly arise due



**Figure 7.** UV-vis spectra (black line) and PL excitation spectra (red line) for GQD1–GQD4 (a–d). The inset images are daylight images and under 365 nm UV irradiation images.

**Table 3.** UV-Vis Spectra Peaks, PLE Peaks, Excitation Peak from Tauc Plot and Band Gap for GQD1–GQD4

	GQD1	GQD2	GQD3	GQD4
$\pi \rightarrow \pi^*$ (nm)	261	279	253	254
$n \rightarrow \pi^*$ (nm)	357	370	365	325
PLE (nm)	354, 370	343, 368	359, 376	361, 403
excitation peaks (nm)	349	340	363	328
band gap (eV)	3.55	3.64	3.41	3.78

to armchair edges and peak at 522 nm due to C–O and C=O functional groups. For GQD2, the peak at 522 nm is significantly reduced, which could be due to decrease in the amount of C–O and C=O functional groups. For GQD3, the amount of oxidation is minimum; the blue luminescence could be due to armchair edges in GQD3.<sup>6</sup> For GQD4, oxidation is again increased and the green emission is due to the presence of C=O and O–C=O functional groups. For GQD1 and GQD4, green luminescence originates due to the presence of oxygen functional groups C–O, C=O, and O–C=O on the surface of GQD1 and GQD4.<sup>48</sup> The synthesis procedure plays a significant role in obtaining the functional groups on the surface of GQDs.<sup>6</sup>

**3.7. Time-Resolved Fluorescence Spectroscopy.** Figure 9 illustrates fluorescence decay curve (along with curve fitting) of GQD1–GQD4. Table 4 depicts the values obtained by time-correlated single photon counting (TCSPC) characterization. Fluorescence decay curves of GQD1–GQD4 are measured using time-correlated single photon counting spectrometer. The fluorescence decay curve is fitted with triexponential function (eq 1), which indicates that fluorescence decay occurs through three relaxation pathways. The red line shows decay curve, and the blue line shows fitted curve. The fitting is performed using the following equation

$$\text{fit} = A + B_1 e^{(-t/\tau_1)} + B_2 e^{(-t/\tau_2)} + B_3 e^{(-t/\tau_3)} \quad (1)$$

where “ $\tau$ ” is the fluorescence lifetime and “ $B$ ” represents amplitude of the corresponding lifetime. The obtained  $\chi^2$  ranges between 1.08 and 1.16. The  $\chi^2$  value in the range of  $1.0 < \chi^2 < 1.2$  was assumed to provide a good fit. Among the three lifetimes, one is due to intrinsic state and the other two are due to the presence of oxygen-rich functional groups on the surface of GQDs. Fluorescence lifetimes of GQDs are recorded at 450 nm for GQD1, GQD2, and GQD3 and at 480 nm for GQD4. The excitation wavelength is 375 nm, which is provided by a diode laser. The fluorescence emission of the surface states exhibit a longer lifetime in comparison to that of the intrinsic state emission. For GQD1–GQD4, exciton lifetimes are ca. 2 ns (ca. 50%), ca. 6 ns (ca. 10%), and ca. 0.5 ns (ca. 40%).

From Table 4, for GQD1–GQD4, three lifetimes are observed as ca. 0.5, 2, and 6 ns. The PLE spectra (Figure 7) depict two peaks representing the two functional groups (armchair edges and oxygen functional groups). Two peaks in PLE curve correspond to TCSPC results (Figure 9), in which the two functional groups have high fluorescence decay time (ca. 2 and 6 ns) in comparison to that of intrinsic state lifetime (ca. 0.5 ns). It is understood that the luminescences of GQD1–GQD4 are primarily dominated by the functional groups present on the surface of GQD1–GQD4. The fluorescence lifetime in nanosecond range indicates that GQD1–GQD4 have singlet-state nature.<sup>49,50</sup>

**3.8. Energy Band Diagram.** Figure 10 illustrates energy band diagrams of GQD1–GQD4. The energy levels are proposed with the help of TEM (Figure 3), UV-vis and PLE (Figure 7), PL (Figure 8), and TCSPC (Figure 9) characterization results. The average size of GQD1–GQD4 plays a crucial role in intrinsic state absorption. As depicted in the UV-vis curve discussed in Figure 7, for GQD1–GQD4,  $\pi$ – $\pi^*$  transition is observed in the range of 253–279 nm with average



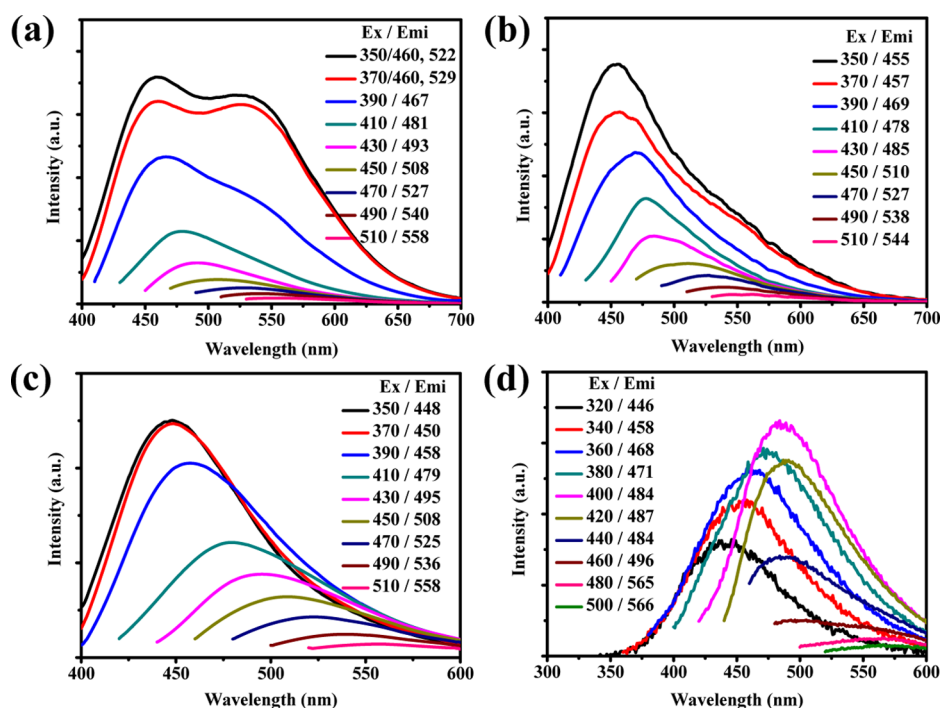


**Figure 8.** Excitation-dependent PL behavior of GQD1–GQD4 (a–d). The insets show excitation wavelengths and their corresponding emission wavelengths.

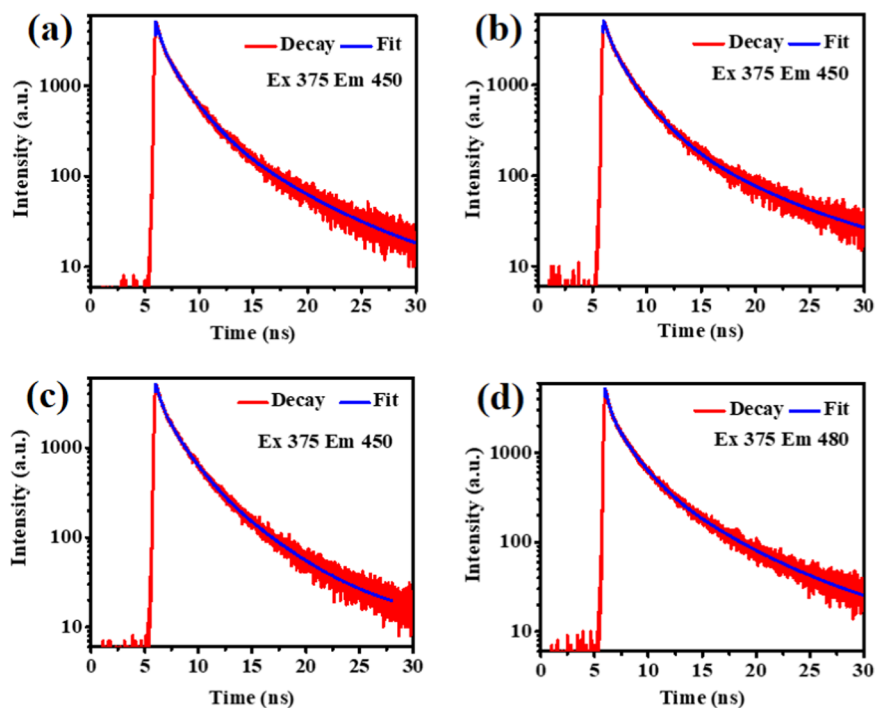


**Figure 9.** Fluorescence decay curves for GQD1–GQD4 (a–d) at 450 and 480 nm measured by TCSPC, excited at 375 nm. The red line shows decay curve, and the blue line shows fitted curve.

size of ca. 2.5 nm (Figure 3). As we can see, in the intrinsic state in Figure 10, due to increase in size of GQD1 (2.5 nm) to GQD2 (3.04 nm), there is an occurrence of red shift. For GQD2 (3.04 nm) to GQD3 (2.24 nm), there is a decrease in size, resulting in blue shift. However, due to slight increase in size from GQD3 (2.24 nm) to GQD4 (2.65 nm), red shift is seen. As depicted in the PLE curve shown in Figure 7, for  $n-\pi^*$  transition, GQD1 shows two peaks at 354 and 370 nm, GQD2

shows two peaks at 343 and 368 nm, GQD3 shows two peaks at 359 and 376 nm, and GQD4 shows two peaks at 361 and 403 nm. These two peaks correspond to two surface states present on the surface of GQD1–GQD4. The energy levels corresponding to these two surface states are shown in Figure 10. The excitation-dependent PL (Figure 8) shows maximum emission in the range of 448–538 nm. PL emission shows two peaks at 454 and 535 nm for GQD1, 448 and 527 nm for

**Table 4.** Excitation Emission Values,  $\chi^2$  Values, Exciton Lifetimes, and Their Corresponding Amplitudes for GQD1–GQD4

	GQD1	GQD2	GQD3	GQD4
Ex/Emi (nm)	375/450	375/450	375/450	375/480
$\chi^2$	1.16	1.15	1.08	1.12
$\tau_1$ (ns)/ $B_1$ (%)	1.9/50	2.1/52	1.9/52	1.9/44
$\tau_2$ (ns)/ $B_2$ (%)	6.21/9	7.2/8	5.7/10	6.3/11
$\tau_3$ (ns)/ $B_3$ (%)	0.51/39	0.63/39	0.49/37	0.42/44

GQD2, 448 nm for GQD3, and 480 and 538 nm for GQD4. The blue luminescence at ca. 450 nm and green luminescence at ca. 530 nm arise due to the two surface states. Figure 2 shows luminescence under 365 nm UV irradiation. GQD1, GQD2, and GQD4 emit blue and green luminescence, whereas GQD3 emits only blue luminescence. Green luminescence is due to the presence of oxygen-rich functional groups, and blue luminescence could be possibly due to the presence of armchair edges.<sup>48,6</sup> For GQD3, the green luminescence is nearly absent due to very low amount of oxygen functional groups. The energy levels corresponding to blue and green luminescence are shown in Figure 10. The fluorescence lifetime decay curve (Figure 9) is fitted with triexponential function. The obtained three lifetimes are 0.5, ca. 2, and ca. 6 ns. The lowest lifetime corresponds to intrinsic state. However, the two higher lifetimes correspond to these two surface states. These two surface states are shown as molecule-like states reported elsewhere.<sup>51</sup> XPS analysis (Figure 4) supports the above discussion regarding the functional groups. However, it is very difficult to figure out the exact surface states experimentally and is beyond the scope of the present work.

#### 4. CONCLUSIONS AND FUTURE DIRECTIONS

In summary, we have developed an easy electrochemical exfoliation strategy to prepare graphene quantum dots (GQDs) and graphene oxide quantum dots (GOQDs). By varying the

alkali hydroxide concentration in the electrolyte, we get GOQDs with tunable oxygen functional groups. A simple electrochemical setup, i.e., with two graphite rods (electrodes), and electrolyte as combination of citric acid and alkali hydroxide is used. Heating the graphite rods at high temperature causes the generation of defects on the surface of graphite rods. Further,  $\text{OH}^-$  ion intercalation, oxygen production, and exfoliation of GQDs form the basis of the mechanism of formation of GQDs. The GQDs and GOQDs have the average size of 2–3 nm and show blue to green fluorescence under 365 nm UV irradiation. Thus, GQDs and GOQDs with tunable oxygen functional groups can be easily prepared by varying the alkali hydroxide concentration in the electrolyte. The easy preparation approach and their unique luminescence properties make them potential candidate for biological applications, such as bioimaging, photodynamic therapy, biosensing, and many others.

#### 5. EXPERIMENTAL SECTION

**5.1. Preparation of GQDs.** Graphite rods (purity > 99.9995%) are purchased from Alfa Aesar (CAS No. 7782-42-5). The graphite rods with a diameter of 3.05 mm and an approximate length of 60 mm are heated in a furnace (at 1050 °C for 5 min) in the presence of air. After 5 min, the graphite rods are allowed to cool at room temperature. Thereafter, the graphite rods are washed with Milli-Q water to remove large particles from the surface of the graphite rods. The graphite rods are then used as anode and cathode, i.e., electrodes to be dipped in the electrolyte. Four types of GQDs are prepared i.e., GQD1–GQD4. For GQD1–GQD4, the electrolyte used is a mixture of citric acid monohydrate (0.1 M) and NaOH (0.15–0.4 M) in Milli-Q water (50 mL). Thereafter, the electrochemical experiments are done with CHI660D Electrochemical Workstation. The separation between the graphite rods is ca. 25 mm. Cyclic voltammetry (CV) is performed prior to performing chronoamperometry. CV is performed with a voltage range of –1 to +1 V, to wet the graphite electrodes. Thereafter,

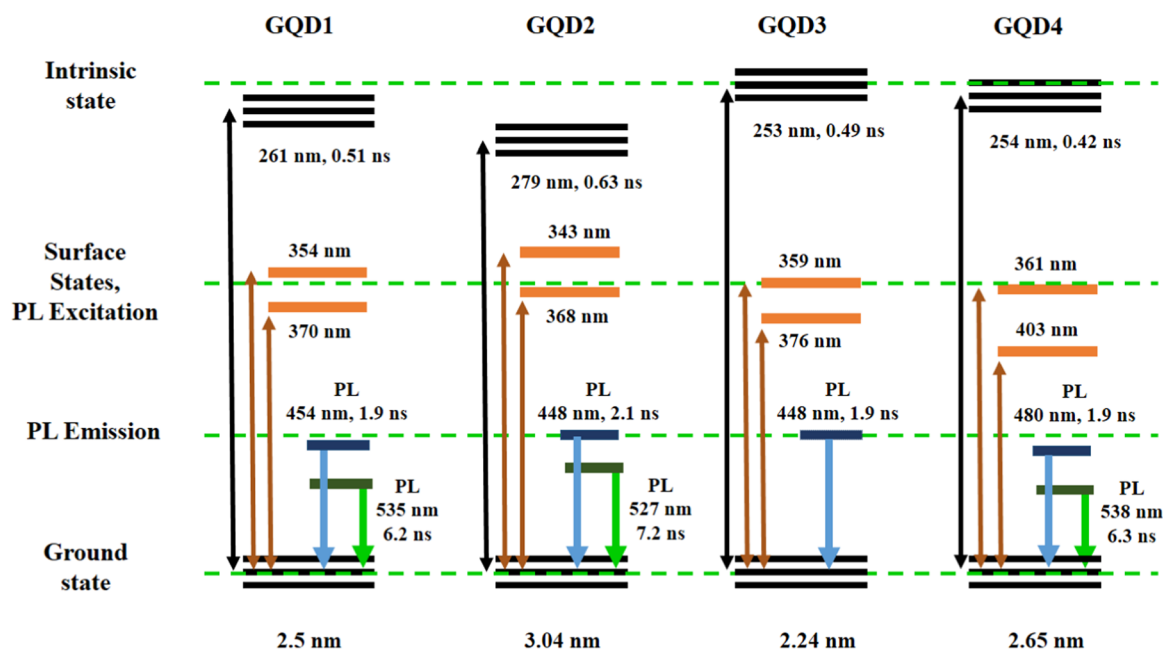


**Figure 10.** Schematic representation of the proposed energy levels of GQD1–GQD4. The intrinsic state depends on size. The surface states determine the optical properties.

chronoamperometry is performed with a voltage of +10 V and a sensitivity ( $I/V$ ) of 0.1 for 30 min. As a result, the color of the electrolyte solution changes from colorless to yellow, which confirms the exfoliation of graphite rod. After completion of this reaction, calcium chloride (0.15 M) is added to the prepared solution. This solution is slightly heated to precipitate calcium citrate. Centrifugation is performed for 15 min at 10 000 rpm twice to separate the calcium citrate precipitate. The supernatant is thereafter filtered through membrane filtration (Himedia, Dialysis Membrane-150, LA401, pore size ca. 2.4 nm) for 7 days to remove salt from the solution.

**5.2. Instruments and Characterization.** UV–vis absorption spectra were recorded on a UV–visible spectrophotometer (Jasco V-650 spectrophotometer, Jasco Int. Pvt. Ltd.). Photoluminescence (PL) studies were performed on a Cary Eclipse fluorescence spectrophotometer (Agilent Technologies). X-ray diffraction patterns were measured on PANalytical X'Pert PRO Model Empyrean X-ray diffractometer (45 kV, 40 mA, Cu  $K\alpha$  radiation). SEM characterization was done using field emission gun-SEM instrument (JEOL JSM-7600F). High-resolution TEM was used to determine particle size, distribution, and morphologies of GQDs using TEM (200 kV, JEOL JEM-2100F). X-ray photoelectron spectroscopy (XPS) measurements were carried out using a scanning XPS microscope (PHI 5000 VersaProbe-II, ULVAC-PHI; Al  $K\alpha$  monochromatic radiation energy, 1486.7 eV). Raman characterization was done with a Raman microscope (LabRAM HR 800 micro-Raman microscope, 514 nm argon laser used with a power of 10 mW). A time-correlated single photon counting (TCSPC) spectrometer (IBH Horiba Jobin Yvon, FluoroCube) was used to measure nanosecond lifetime. GQDs were excited with a 375 nm diode laser (Horiba NanoLED), and the decay curves were fitted using IBH DAS 6.2 software.

## ■ ASSOCIATED CONTENT

### Supporting Information

The Supporting Information is available free of charge on the ACS Publications website at DOI: 10.1021/acsomega.7b01539.

TEM characterization (Table S1), Raman spectroscopy (Table S2), and PL characterization (Table S3) for GQD1–GQD4 (PDF)

## ■ AUTHOR INFORMATION

### Corresponding Author

\*E-mail: dhiren@iitb.ac.in.

### ORCID

Satyaprakash Ahirwar: 0000-0001-6390-673X

Sudhanshu Mallick: 0000-0002-9744-8746

Dhirendra Bahadur: 0000-0002-5092-6624

### Notes

The authors declare no competing financial interest.

## ■ ACKNOWLEDGMENTS

Financial support from Nano Mission, Department of Science and Technology (DST), Government of India, is greatly acknowledged. The authors acknowledge Industrial Research and Consultancy Center (IRCC) Central Facility, IIT Bombay; Sophisticated Analytical Instrument Facility (SAIF), IIT Bombay for TEM, Raman, ESR, confocal spectroscopy, and SEM facility; and Centre of Excellence in Nanoelectronics (CEN), IIT Bombay, for XPS facility. They thank Prof. A.

Datta, Department of Chemistry, IIT Bombay, for TCSPC facility.

## ■ REFERENCES

- (1) Geim, A. K. Graphene: status and prospects. *Science* **2009**, *324*, 1530–1534.
- (2) Rao, C. N. R.; Sood, A. K.; Subrahmanyam, K. S.; Govindaraj, A. Graphene: The New Two-Dimensional Nanomaterial. *Angew. Chem., Int. Ed.* **2009**, *48*, 7752–7777.
- (3) Ponomarenko, L. A.; Schedin, F.; Katsnelson, M. I.; Yang, R.; Hill, E. W.; Novoselov, K. S.; Geim, A. K. Chaotic dirac billiard in graphene quantum dots. *Science* **2008**, *320*, 356–358.
- (4) Girit, C. O.; Meyer, J. C.; Erni, R.; Rossell, M. D.; Kisielowski, C.; Yang, L.; Park, C. H.; Crommie, M. F.; Cohen, M. L.; Louie, S. G.; Zettl, A. Graphene at the edge: stability and dynamics. *Science* **2009**, *323*, 1705–1708.
- (5) Ritter, K. A.; Lyding, J. W. The influence of edge structure on the electronic properties of graphene quantum dots and nanoribbons. *Nat. Mater.* **2009**, *8*, 235–242.
- (6) Zhu, S.; Song, Y.; Zhao, X.; Shao, J.; Zhang, J.; Yang, B. The photoluminescence mechanism in carbon dots (graphene quantum dots, carbon nanodots, and polymer dots): current state and future perspective. *Nano Res.* **2015**, *8*, 355–381.
- (7) Shen, J.; Zhu, Y.; Yang, X.; Li, C. Graphene quantum dots: emergent nanolights for bioimaging, sensors, catalysis and photovoltaic devices. *Chem. Commun.* **2012**, *48*, 3686–3699.
- (8) Li, L.; Wu, G.; Yang, G.; Peng, J.; Zhao, J.; Zhu, J. J. Focusing on luminescent graphene quantum dots: current status and future perspectives. *Nanoscale* **2013**, *5*, 4015–4039.
- (9) Tan, X.; Li, Y.; Li, X.; Zhou, S.; Fan, L.; Yang, S. Electrochemical synthesis of small-sized red fluorescent graphene quantum dots as a bioimaging platform. *Chem. Commun.* **2015**, *51*, 2544–2546.
- (10) Bacon, M.; Bradley, S. J.; Nann, T. Graphene quantum dots. *Part. Part. Syst. Charact.* **2014**, *31*, 415–428.
- (11) Wen, J.; Xu, Y.; Li, H.; Lu, A.; Sun, S. Recent applications of carbon nanomaterials in fluorescence biosensing and bioimaging. *Chem. Commun.* **2015**, *51*, 11346–11358.
- (12) Song, S. H.; Jang, M. H.; Chung, J.; Jin, S. H.; Kim, B. H.; Hur, S. H.; Yoo, S.; Cho, Y. H.; Jeon, S. Highly efficient light-emitting diode of graphene quantum dots fabricated from graphite intercalation compounds. *Adv. Opt. Mater.* **2014**, *2*, 1016–1023.
- (13) Xie, M.; Su, Y.; Lu, X.; Zhang, Y.; Yang, Z.; Zhang, Y. Blue and green photoluminescence graphene quantum dots synthesized from carbon fibers. *Mater. Lett.* **2013**, *93*, 161–164.
- (14) Pan, D.; Zhang, J.; Li, Z.; Wu, M. Hydrothermal route for cutting graphene sheets into blue-luminescent graphene quantum dots. *Adv. Mater.* **2010**, *22*, 734–738.
- (15) Li, Y.; Hu, Y.; Zhao, Y.; Shi, G.; Deng, L.; Hou, Y.; Qu, L. An electrochemical avenue to green-luminescent graphene quantum dots as potential electron-acceptors for photovoltaics. *Adv. Mater.* **2011**, *23*, 776–780.
- (16) Swain, A. K.; Li, D.; Bahadur, D. UV-assisted production of ferromagnetic graphitic quantum dots from graphite. *Carbon* **2013**, *57*, 346–356.
- (17) Kumawat, M. K.; Thakur, M.; Gurung, R. B.; Srivastava, R. Graphene Quantum Dots from *Mangifera indica*: Application in Near-Infrared Bioimaging and Intracellular Nanothermometry. *ACS Sustainable Chem. Eng.* **2017**, *5*, 1382–1391.
- (18) Gu, J.; Zhang, X.; Pang, A.; Yang, J. Facile synthesis and photoluminescence characteristics of blue-emitting nitrogen-doped graphene quantum dots. *Nanotechnology* **2016**, *27*, No. 165704.
- (19) Dong, Y.; Shao, J.; Chen, C.; Li, H.; Wang, R.; Chi, Y.; Lin, X.; Chen, G. Blue luminescent graphene quantum dots and graphene oxide prepared by tuning the carbonization degree of citric acid. *Carbon* **2012**, *50*, 4738–4743.
- (20) Chua, C. K.; Sofer, Z.; Simek, P.; Jankovsky, O.; Klimova, K.; Bakardjieva, S.; Kuckova, S. H.; Pumera, M. Synthesis of strongly fluorescent graphene quantum dots by cage-opening buckminsterfullerene. *ACS Nano* **2015**, *9*, 2548–2555.



- (21) Umrao, S.; Jang, M. H.; Oh, J. H.; Kim, G.; Sahoo, S.; Cho, Y. H.; Srivastva, A.; Oh, I. K. Microwave bottom-up route for size-tunable and switchable photoluminescent graphene quantum dots using acetylacetone: new platform for enzyme-free detection of hydrogen peroxide. *Carbon* **2015**, *81*, 514–524.
- (22) Tang, L.; Ji, R.; Cao, X.; Lin, J.; Jiang, H.; Li, X.; Teng, K. S.; Luk, C. M.; Zeng, S.; Hao, J.; Lau, S. P. Deep ultraviolet photoluminescence of water-soluble self-passivated graphene quantum dots. *ACS Nano* **2012**, *6*, 5102–5110.
- (23) Zhu, H.; Wang, X.; Li, Y.; Wang, Z.; Yang, F.; Yang, X. Microwave synthesis of fluorescent carbon nanoparticles with electrochemiluminescence properties. *Chem. Commun.* **2009**, *34*, 5118–5120.
- (24) Liu, R.; Wu, D.; Feng, X.; Mullen, K. Bottom-up fabrication of photoluminescent graphene quantum dots with uniform morphology. *J. Am. Chem. Soc.* **2011**, *133*, 15221–15223.
- (25) Wu, J.; Pisula, W.; Mullen, K. Graphenes as potential material for electronics. *Chem. Rev.* **2007**, *107*, 718–747.
- (26) Kundu, S.; Yadav, R. M.; Narayanan, T. N.; Shelke, M. V.; Vajtai, R.; Ajayan, P. M.; Pillai, V. K. Synthesis of N, F and S co-doped graphene quantum dots. *Nanoscale* **2015**, *7*, 11515–11519.
- (27) Liu, F.; Jang, M. H.; Ha, H. D.; Kim, J. H.; Cho, Y. H.; Seo, T. S. Facile synthetic method for pristine graphene quantum dots and graphene oxide quantum dots: origin of blue and green luminescence. *Adv. Mater.* **2013**, *25*, 3657–3662.
- (28) Valappil, M. O.; Anil, A.; Shaijumon, M.; Pillai, V. K.; Alwarappan, S. A Single-Step Electrochemical Synthesis of Luminescent WS<sub>2</sub> Quantum Dots. *Chem. - Eur. J.* **2017**, *23*, 9144–9148.
- (29) Gopalakrishnan, D.; Damien, D.; Li, B.; Gullappalli, H.; Pillai, V. K.; Ajayan, P. M.; Shaijumon, M. M. Electrochemical synthesis of luminescent MoS<sub>2</sub> quantum dots. *Chem. Commun.* **2015**, *51*, 6293–6296.
- (30) Lee, S. H.; Seo, S. D.; Jin, Y. H.; Shim, H. W.; Kim, D. W. A graphite foil electrode covered with electrochemically exfoliated graphene nanosheets. *Electrochem. Commun.* **2010**, *12*, 1419–1422.
- (31) Lu, J.; Yang, J. X.; Wang, J.; Lim, A.; Wang, S.; Loh, K. P. One-pot synthesis of fluorescent carbon nanoribbons, nanoparticles, and graphene by the exfoliation of graphite in ionic liquids. *ACS Nano* **2009**, *3*, 2367–2375.
- (32) Parvez, K.; Wu, Z. S.; Li, R.; Liu, X.; Graf, R.; Feng, X.; Mullen, K. Exfoliation of graphite into graphene in aqueous solutions of inorganic salts. *J. Am. Chem. Soc.* **2014**, *136*, 6083–6091.
- (33) Beck, F.; Junge, H.; Krohn, H. Graphite intercalation compounds as positive electrodes in galvanic cells. *Electrochim. Acta* **1981**, *26*, 799–809.
- (34) Beck, F.; Jiang, J.; Krohn, H. Potential oscillation during galvanostatic overoxidation of graphite in aqueous sulphuric acids. *J. Electroanal. Chem.* **1995**, *389*, 161–165.
- (35) Shinde, D. B.; Majumder, M.; Pillai, V. K. Counter-ion Dependent, Longitudinal Unzipping of Multi-Walled Carbon Nanotubes to Highly Conductive and Transparent Graphene Nanoribbons. *Sci. Rep.* **2014**, *4*, No. 4363.
- (36) John, R.; Shinde, D. B.; Liu, L.; Ding, F.; Xu, Z.; Vijayan, C.; Pillai, V. K.; Pradeep, T. Sequential Electrochemical Unzipping of Single-Walled Carbon Nanotubes to Graphene Ribbons Revealed by in Situ Raman Spectroscopy and Imaging. *ACS Nano* **2014**, *8*, 234–242.
- (37) Shinde, D. B.; Pillai, V. K. Electrochemical Resolution of Multiple Redox Events for Graphene Quantum Dots. *Angew. Chem., Int. Ed.* **2013**, *52*, 2482–2485.
- (38) Dong, Y.; Pang, H.; Yang, H. B.; Guo, C.; Shao, J.; Chi, Y.; Li, C. M.; Yu, T. Carbon-based dots co-doped with nitrogen and sulfur for high quantum yield and excitation-independent emission. *Angew. Chem., Int. Ed.* **2013**, *52*, 7800–7804.
- (39) Kalita, H.; Mohapatra, J.; Pradhan, L.; Mitra, A.; Bahadur, D.; Aslam, M. Efficient synthesis of rice based graphene quantum dots and their fluorescent properties. *RSC Adv.* **2016**, *6*, 23518–23524.
- (40) Feng, Y.; Zhao, J.; Yan, X.; Tang, F.; Xue, Q. Enhancement in the fluorescence of graphene quantum dots by hydrazine hydrate reduction. *Carbon* **2014**, *66*, 334–339.
- (41) Fan, T.; Zeng, W.; Tang, W.; Yuan, C.; Tong, S.; Cai, K.; Liu, Y.; Huang, W.; Min, Y.; Epstein, A. J. Controllable size-selective method to prepare graphene quantum dots from graphene oxide. *Nanoscale Res. Lett.* **2015**, *10*, 55.
- (42) Qu, D.; Zheng, M.; Zhang, L.; Zhao, H.; Xie, Z.; Jing, X.; Haddad, R. E.; Fan, H.; Sun, Z. Formation mechanism and optimization of highly luminescent N-doped graphene quantum dots. *Sci. Rep.* **2014**, *4*, No. 5294.
- (43) Shih, Y. W.; Tseng, G. W.; Hsieh, C. Y.; Li, Y. Y.; Sakoda, A. Graphene quantum dots derived from platelet graphite nanofibers by liquid-phase exfoliation. *Acta Mater.* **2014**, *78*, 314–319.
- (44) Zhang, R.; Liu, Y.; Yu, L.; Li, Z.; Sun, S. Preparation of high-quality biocompatible carbon dots by extraction, with new thoughts on the luminescence mechanisms. *Nanotechnology* **2013**, *24*, No. 225601.
- (45) Tetsuka, H.; Asahi, R.; Nagoya, A.; Okamoto, K.; Tajima, I.; Ohta, R.; Okamoto, A. Optically tunable amino-functionalized graphene quantum dots. *Adv. Mater.* **2012**, *24*, 5333–5338.
- (46) Kudin, K. N.; Ozbas, B.; Schniepp, H. C.; Prud'homme, R. K.; Aksay, I. A.; Car, R. Raman spectra of graphite oxide and functionalized graphene sheets. *Nano Lett.* **2008**, *8*, 36–41.
- (47) Sobon, G.; Sotor, J.; Jagiello, J.; Kozinski, R.; Zdrojek, M.; Holdynski, M.; Paletko, P.; Boguslawski, J.; Lipinska, L.; Abramski, K. M. Graphene oxide vs reduced graphene oxide as saturable absorbers for Er-doped passively mode-locked fiber laser. *Opt. Express* **2012**, *20*, 19463–19473.
- (48) Wang, L.; Zhu, S. J.; Wang, H. Y.; Qu, S. N.; Zhang, Y. L.; Zhang, J. H.; Chen, Q. D.; Xu, H. L.; Han, W.; Yang, B.; Sun, H. B. Common origin of green luminescence in carbon nanodots and graphene quantum dots. *ACS Nano* **2014**, *8*, 2541–2547.
- (49) Zhu, S.; Shao, J.; Song, Y.; Zhao, X.; Du, J.; Wang, L.; Wang, H.; Zhang, K.; Zhang, J.; Yang, B. Investigating the surface state of graphene quantum dots. *Nanoscale* **2015**, *7*, 7927–7933.
- (50) Ge, J.; Lan, M.; Zhou, B.; Liu, W.; Guo, L.; Wang, H.; Jia, Q.; Niu, G.; Huang, X.; Zhou, H.; Meng, X.; Wang, P.; Lee, C. S.; Zhang, W.; Han, X. A graphene quantum dot photodynamic therapy agent with high singlet oxygen generation. *Nat. Commun.* **2014**, *5*, No. 4596.
- (51) Wang, L.; Zhu, S. J.; Wang, H. Y.; Wang, Y. F.; Hao, Y. W.; Zhang, J. H.; Chen, Q. D.; Zhang, Y. L.; Han, W.; Yang, B.; Sun, H. B. Unraveling Bright Molecule-Like State and Dark Intrinsic State in Green-Fluorescence Graphene Quantum Dots via Ultrafast Spectroscopy. *Adv. Opt. Mater.* **2013**, *1*, 264–271.